ELSEVIER

Contents lists available at ScienceDirect

Additive Manufacturing

journal homepage: www.elsevier.com/locate/addma





Impact of binder on part densification: Enhancing binder jetting part properties through the fabrication of shelled geometries

Kazi Moshiur Rahman^a, Amanda Wei^a, Hadi Miyanaji^a, Christopher B. Williams^{a,*}

a Design, Research, and Education for Additive Manufacturing Systems Laboratory, Department of Mechanical Engineering, Virginia Tech, Blacksburg, VA 24061, USA

ARTICLE INFO

Keywords:
Binder Jetting
Additive Manufacturing
Shell Printing
Binder Saturation
Densification
Copper

ABSTRACT

In binder jetting (BJT) additive manufacturing (AM), jetted liquid binder binds powder particles and provides structural integrity to the printed green parts. Following printing, the binder is pyrolyzed before densification to final part. While the effects of binder saturation on the green part quality have been explored, the study of the impact of binder on part densification and subsequent part properties is limited. In this study, the impact of binder on densification is studied through a new approach of binder jetting termed as "shell printing" to vary the amount of binder content in a green part. In this approach, binder is only deposited around the part surface, which effectively traps packed powders inside the bound shell geometry. Post-process sintering consolidates both bound (printed shell) and unbound powders and densifies the part. Manipulation of the shell thickness enables exploration of the effects of binder content on process-structure-property relationships. Using pure copper as an exemplar material, and analyzing parts with varying shell thicknesses, it was found that shell printing significantly affects green part density (3.7% increase), final part density (~5% increase), grain size (~290% increase) and tensile strength (8.84% increase) when compared to traditional strategies of homogeneous binder placement. While the traditional binding approach improves green part strength and reduces part slumping during sintering, it also hinders densification, constrains grain growth, and induces porosity at the grain boundaries, as compared to the shell printing approach.

1. Introduction

1.1. Binder jetting additive manufacturing

Binder jetting (BJT) is a powder bed based additive manufacturing (AM) process capable of fabricating highly complex parts at high throughput and low cost [1,2]. A typical metal BJT process consists of two major steps: (i) green part formation (part shaping) and (ii) post-process part densification. Metal powder is spread to a desired layer thickness on a build-bed and liquid droplets of a polymeric binder are selectively jetted from an inkjet printhead on to the powder to selectively bind the particles. Another layer of powder is spread, printed, and bonded with the previous layer. This process is repeated until a 3D shape of the desired part geometry is fully realized. The build-bed, along with the printed parts, is then subjected to low temperature (\sim 150 °C) heat to cure the deposited binder, and the green parts are then removed from the build-bed and depowdered. Due to limited particle packing, the as-printed (green) parts feature significant amount of porosity (typically in the range of 50–60% [2]) and are still fragile. To achieve higher

density and strength, the parts undergo a post-process thermal treatment that features a burnout step (at temperature $\sim\!450~^\circ\text{C})$ to pyrolyze the binder, followed by a high temperature sintering step.

1.2. Impact of binder in BJT-AM

A key component of BJT is the binder itself, which defines the formation of green parts and significantly influences the resulting part properties. Liquid droplets of binder wet the particles and fill in the interstitial pores by various infiltration mechanisms (spreading and penetration) that are driven by capillary pressure [3,4]. As such, the binder must meet key requirements of chemical stability [2], having the proper rheology (surface tension and viscosity) [5], wettability with the powders [6], and adequate binding strength [2]. In the most advanced BJT systems where polymeric binders (solvent or water-based) are almost exclusively used, the solvent is evaporated through in-situ heating, and polymer chains attach and form pendular bonds between particles during the curing process, which imparts strength to the green part.

E-mail address: cbwill@vt.edu (C.B. Williams).

^{*} Corresponding author.

Usually, the binder content in a powder bed is expressed by the binder saturation, which is defined as the ratio of the binder volume to powder bed pore volume. It is a user-specified process parameter that is dependent on measurement of droplet volume and powder packing. From this, the BJT system automatically determines the corresponding droplet spacings for a homogeneous distribution of binder across each part layer. A sufficient binder saturation ratio and a proper wetting and penetration need to occur to fabricate a green part with sufficient mechanical strength and structural stability to survive depowdering. In addition to controlling the green parts' density and strength, binder saturation also influences the final part densification and porosity distribution [7-9]. A low binder saturation can cause layer delamination and high amount of porosity in both green and sintered parts; whereas, a high binder saturation may lead to wetting of excessive amount of powders beyond specified powder volume (known as "bleeding"), resulting in inaccurate part geometries [10,11]. Powder bed characteristics, processing parameters (e.g., layer thickness, drying time) and the desired part properties dictate the required level of binder saturation. In this regard, researchers have determined the appropriate saturation through study of empirical processing-properties relations [12-15]. A physics-based model has also been proposed by Miyanaji et al. [4] that predicts the powder bed capillary pressure at equilibrium, which is then used to determine the actual equilibrium saturation level by calibrating with an empirical capillary pressure-saturation curve.

In general, increasing binder saturation increases the strength and enhances integrity of a printed green part. Lu et al. [16] printed fine mesh structures using TiNiHf shape memory alloy powder with varying saturation ratio (55%, 110%, 170%). Parts with lowest saturation were fragile, while parts with higher saturation demonstrated higher breaking strength. In another study, Lecis et al. [17] achieved higher bending strength of stainless steel 316 L green parts with higher saturation. Vaezi et al. [12] evaluated the surface quality, geometric accuracy, and mechanical strength of parts printed with a plaster-based powder (ZP102). Enhanced tensile and flexural strength were achieved by increasing binder saturation from 90% to 125%, although with the expense of geometric accuracy and surface quality. Enneti et al. [13] studied the effect of binder saturation and layer thickness on the transverse rupture strength of WC-12%Co printed green parts. Strength was found to increase with increasing saturation ratio for all layer thicknesses evaluated.

Researchers have also studied the effects of saturation ratio to understand its impact on printed final part properties. Past studies have shown that increasing binder saturation can increase sintered density; however, there is an inflection point at which density decreases beyond a certain saturation level. Mostafaei et al. [7] studied the effects of binder saturation in the range of 60-250% on WC-Co composite powders, where the high binder saturations caused remnant pores in the sintered parts. The relative densities increased for saturation of 100-200% but decreased for saturations of 225%- 250% due to high amount of porosity. Jiang et al. [8] explored the influence of binder saturation on gas-atomized and water-atomized Inconel 615 in a comparative study. The gas-atomized specimens demonstrated an increase in relative density with saturations between 50% and 80%; saturations over 100% showed lower relative density. On the other hand, water-atomized specimens demonstrated an increase in relative density with saturations between 50% and 60%, and a decrease when exceeding saturation beyond 70%. Similar trends were observed in the mechanical properties (via microhardness) of the specimens. Shrestha et al. [18] tested binder saturation of 35%, 70%, 100% on the transverse rupture strength of stainless steel 316 L in their optimization study and reported that 70% saturation provided the maximum strength, when the layer thickness, roller speed, and feed-to-powder ratio were $100 \mu m$, 6mm/s, and 3:1, respectively. In another study with stainless steel 316 L, Lecis et al. [17] found that relative density decreased as binder saturation increased from 55% to 70%. While these studies have experimentally related binder saturation and densification, the fundamental

understanding of the impact of binder on part densification and final part properties is limited.

Researchers have hypothesized that carbon residue from binder pyrolysis could potentially inhibit sintering densification by limiting particle neck formation and induce porosity in the final part [2,19]. In addition, this residue can act as an impurity in the final part. As such, many researchers have sought to mitigate these effects by exploring polymer-free binder formulation including nano-particles suspension binder [9,20–22]. However, these binders have processing difficulties including high cost and nozzle clogging [2]; therefore, polymeric binder is the most prevalently used binder due to its compatibility and utility.

Prior research into the effects of (homogenously distributed) binder on densification have shown contradictory results; therefore, further research into binder's impact on process-structure-property relationships in needed. With this aim, this work examines a new technique of varying the binder content in the green part and the subsequent effects on final part properties. The results provide insights into enhancing part properties through proper utilization of binder.

1.3. Shell printing

In this study, the authors explore a new approach of BJT termed as "shell printing" that balances the need of binder for part shape definition while also simultaneously reducing the use of binder to enhance part densification. As shown in Fig. 1, the original solid model of the part is "shelled" with a prescribed thickness, with the inside kept as hollow. The shelled geometry is then printed wherein only the shell region features binder and unbound, packed powders are trapped inside. The printed, shelled, green part is then sintered, resulting in a uniform solid part.

This approach effectively eliminates binder from the "core" of the part and relies only on the jetted binder within the shell to provide green part strength. It is hypothesized that the trapped unbound powders in the center of the part geometry will have enhanced densification due to the absence of any binder phase, as this eliminates any possibility of binder residue inhibiting particle neck formation. The unbound particles will only need to overcome the interstitial spaces for densification.

1.4. Novelty of present work

While the work of the present study was ongoing, a similar "shell printing" approach has been recently examined in laser powder bed fusion (L-PBF) AM process [23]. In addition, a patent [24] has been filed for both L-PBF and BJT as a means of productivity enhancement. In the L-PBF work, Du Plessis et al. [23] used shelled geometries to print metal parts and then consolidated the unmelted interior powders using hot-isostatic-pressing (HIP). Although this approach improved the production rate, part distortion became a concern during the HIP process and required compensation. In the BJT patent, Prichard et al. [24] demonstrated improvement in the sinter-HIP final density by using shell geometries. While the benefits were noted, a thorough examination of shell thickness effects on density and microstructure were not presented.

In comparison, the present work is focused on the study of process-structure-property relations influenced by the shell printing approach. Fundamentally, the authors look to understand the effects of variation of binder content on part densification and final part properties. Additionally, the authors present the shell printing approach as a means of enhancing the final part properties. The effects of shell thickness on part density (green and sintered) and shrinkage, pore morphology and distribution, grain microstructure, mechanical strength, residual binder content, and overall stability are studied.

Fig. 1. Schematic of the shell printing process chain.

2. Materials and methods

2.1. Powder materials and characterization

In this study, all the experimental specimens were fabricated using gas atomized pure copper powders supplied by Mitsui Mining and Smelting Co., Japan. Powder packing density is a crucial characteristic in BJT, which is a determining factor of green part density. Prior research suggested that using bimodal powder size distribution over mono-size powders is beneficial for higher packing density of the powder bed [25,26]. Following this, copper powders with nominally 5 µm and 30 µm size were mixed at a volume ratio of 27:73. To ensure homogeneity of the mixture, the powder container was subjected to a rotating roller shaker at a low rpm (~20) for 4 h. A JEOL IT-500HR scanning electron microscope was used to evaluate the powders' morphology. As shown in Fig. 2, both powders feature mostly spherical particles, which is beneficial for powder flowability and packing density [27].

The packing density of the powder mixture in the powder bed was measured from printed rectangular cups using the method proposed by Elliott et al. [28]. Measurements were taken from cups printed on both edges of the build box to account for potential variation due to roller compaction. The packing density of the powders was found to be 55%.

2.2. Specimen design

Rectangular test coupons ($27 \times 9 \times 4.5 \text{ mm}^3$) and tensile specimens (according to ASTM B925 [29]) were designed to evaluate density and tensile strength, respectively. A cantilevered test specimen was designed (inspired by [9]) to evaluate the stability (slumping) of the parts. In addition to printing the specimens as "controls" in traditional approach in which binder is spread homogeneously, these geometries were printed as shelled geometries (as shown in Fig. 3) of varying shell thicknesses

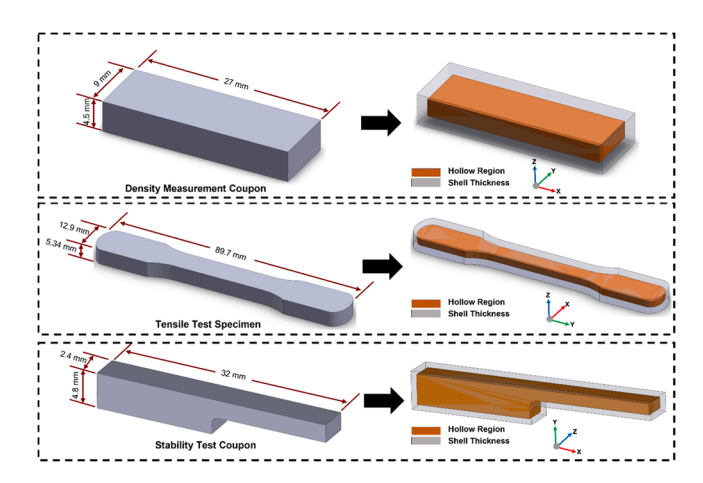


Fig. 3. Design of density, tensile, and stability test specimens (left) original CAD, (right) Shelled CAD (shell thickness was made transparent for convenience of visibility of the hollow region inside).

(0.50 mm, 1.00 mm, and 1.50 mm).

In the test specimens, the volume of powders in the printed shell receiving binder is termed as "bound" and the trapped powders inside the shelled specimens are termed as "unbound". The corresponding bound and unbound volume of powders in each type of specimen are listed in Table 1. It is noted that the tensile and stability specimens with 1.50 mm shell thickness had insufficient unbound volume with the designed specimen dimensions; therefore, were not evaluated.

2.3. Green part fabrication

An ExOne (a Desktop Metal company) Innovent+ BJT system with

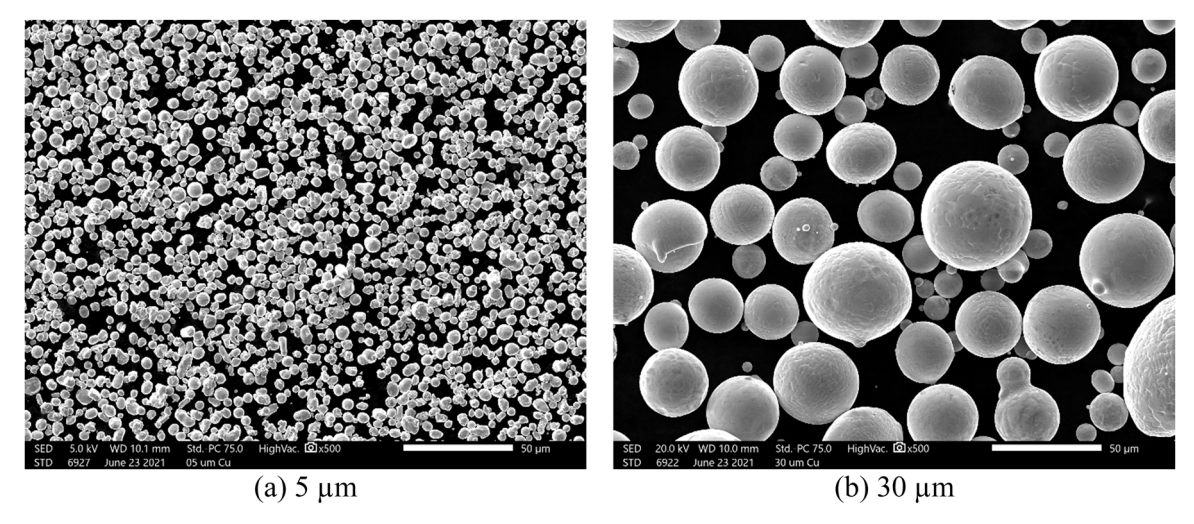


Fig. 2. SEM image of the copper powders used in present study (a) 5 μ m, (b) 30 μ m.

Table 1Volume (%) of bound and unbound powders in test specimens.

| Shell Thickness, t _{shell} (mm) | Density Coupons | | Tensile Specimens | | Stability Specimens | |
|--|------------------|--------------------|-------------------|--------------------|---------------------|--------------------|
| | Bound Volume (%) | Unbound Volume (%) | Bound Volume (%) | Unbound Volume (%) | Bound Volume (%) | Unbound Volume (%) |
| 0 | 100 | 0 | 100 | 0 | 100 | 0 |
| 0.50 | 34.19 | 65.81 | 28.15 | 71.85 | 52.16 | 47.48 |
| 1.00 | 61.15 | 38.85 | 51.25 | 48.76 | 82.25 | 17.75 |
| 1.50 | 80.35 | 19.65 | | | | |

ExOne Aquafuse binder was used to fabricate all of the green parts. The Innovent+ BJT system used in this research recoats each layer by first dispensing powder onto the build box via a vibrating hopper (actuated by an ultrasonic vibrational device), which is then spread by a single counter-rotating roller. The process parameters used to print the parts are given in Table 2. A 50 µm layer thickness was chosen to print all the green parts, which was deemed as the smallest feasible layer thickness for the particles used in this study (i.e., at least one diameter of the largest particle [30]). The powder bed temperature was maintained at 60 °C during all the prints. A 100% binder saturation was chosen to ensure strong particle bonding. The ultrasonic intensity, recoat speed, and roller speed were experimentally proven to provide acceptable prints in preliminary studies [31]. The in-situ layer drying time that was used for printing of fully saturated control (no-shell) parts was found to be unsuitable for shelled parts; the excess drying time for reduced amount of liquid binder resulted in layer warping. To solve this issue, the drying time was adjusted between 15 and 40 s for the different shell thicknesses. The specimens were oriented on the build bed as indicated in Fig. 3, where X is the recoating direction, Y is the jetting direction, and Z being the build direction. A cross-sectional layer with deposited binder in the "shell" while packed powders being trapped inside is shown in Fig. 4. Several batches of test specimens were printed, and the specimens were randomly positioned within the build bed across different batches to minimize the potential effects caused by variable powder packing density in the build box (as observed in [28]). Batch-to-batch variation between similar specimens were statistically insignificant (according to t-tests performed).

2.4. Post-processing

All printed parts were thermally cured at 120 °C temperature for 120 min, followed by depowdering using compressed air. Binder burnout and solid state sintering were performed together in a box furnace (CM Furnaces) with a reducing atmosphere of 100% hydrogen using the heat treatment profile shown in Fig. 5, based on authors' previous studies on BJT of copper [31,32]. A constant 5 °C/min heating rate was used in all the heating ramps. An isothermal dwell of 60 min at 450 °C was used for binder burnout and a final isothermal dwell of 180 min was performed at the peak temperature of 1075 °C, followed by furnace cooling.

2.5. Part characterization

Green part density was calculated by using the weight and

Table 2
BJT process parameters used to print all parts.

| Parameter | Value |
|-----------------------------|-------|
| Layer Thickness (µm) | 50 |
| Binder Droplet Size (pL) | 30 |
| Binder Saturation Ratio (%) | 100 |
| Ultrasonic Intensity (%) | 25% |
| Recoat Speed (mm/sec) | 15 |
| Roller Speed (rpm) | 300 |
| Bed Temperature (°C) | 60 |
| Layer Drying Time (sec) | 15-40 |

dimensions of the green parts, measured by a digital scale (+/- 0.0001~g) and a caliper (+/- 0.01~mm), respectively. Sintered density was measured using immersion technique based on Archimedes' principle, according to ASTM B962 [33]. The specimens were oil impregnated in a vacuum for at least 30 min to remove trapped air and to close all the surface connected porosity before performing the Archimedes tests in water. At least five specimens were measured for each shell thickness. Both the green and sintered density were normalized using the bulk density of copper at room temperature (8.96 g/cm³) to calculate the relative density of the parts.

Some of the sintered density specimens were sectioned and polished to evaluate the pore morphology and distribution in bound (shell) and unbound (trapped powders) regions. Microscopy was performed on the polished specimens using a Zeiss AxioImager A2m upright microscope. The pore size was measured using ImageJ software. The polished specimens were etched using nitric acid solutions to optically activate the grain microstructures. The line intercept method in ImageJ was used to measure the grain size. Four microscopic images of the grain microstructures were used to determine the grain size; the pixel to micron ratio of two images were 3.69 and other two images were 1.845.

Uniaxial tensile tests were performed on the printed tensile specimens in an Instron 5984 system with a 50 kN load cell at a constant extension rate of 1.00 mm/min and a gauge length of 34 mm. The tensile strength data for each printed specimen is represented from an average of at least five specimens.

An FEI Quanta 600 FEG environmental scanning electron microscope (ESEM) equipped with energy-dispersive spectroscopy (EDS) was used to analyze the material composition in the parts. Additionally, a Bruker Q4 Tasman Advanced CCD-based optical emission spectrometer was used to perform spectroscopy on the specimens. At least three measurements were taken on each specimen to evaluate and compare their residual carbon content.

3. Results and discussion

3.1. Density

The green and sintered densities of the parts as a function of shell thickness are shown in Fig. 6. The corresponding nominal volume of the unbound powders in each type of shell thickness parts are plotted in the secondary vertical axis. The error bars in the plots correspond to one standard deviation from the mean density value.

It is observed that green part density increases as the shell thickness (i.e., overall binder content) decreases (Fig. 6(a)). The control parts (with no-shell) demonstrated the lowest green density (55.67%) among the specimens measured, whereas the 0.50 mm shell thickness parts showed the highest green density (59.37%). The green density differences among parts with different shell thickness were found to be statistically significant (p-value < 0.05). Prior understanding suggests that surface tension induced particle bonding may lead to higher green density in the control parts, contrary to the observed results in this study. It is hypothesized that the momentum transfer from droplets' impact on the powder bed may have caused crater formation, particle ejection, and rearrangements during binder-powder interaction [34]. These microscopic events could lead to lower green densities in parts with higher binder content.

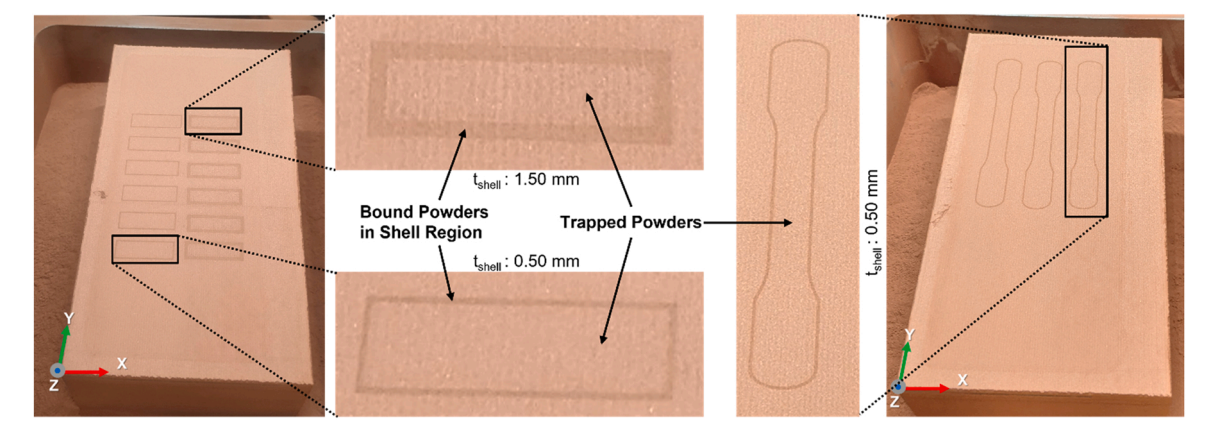


Fig. 4. Printing of a cross-sectional layer showing bound (shell) and unbound (trapped powders) regions in density (left) and tensile (right) specimens.

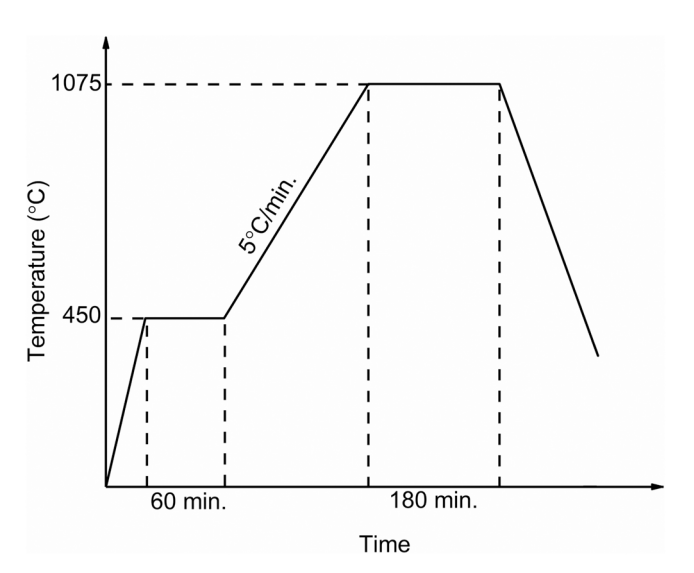


Fig. 5. Heat treatment profile used for sintering of the specimens.

Significant improvement in sintered density was observed in shelled parts compared to the control parts (i.e., no-shell), as shown in Fig. 6(b). The sintered density increased as the shell thickness decreased with statistical significance (p-value < 0.05) among specimens with different shell thickness. The parts with 0.50 mm shell thickness demonstrated the highest density (93.30%), which is 4.58% higher than the control parts density (88.72%). It is important to note that all these parts were

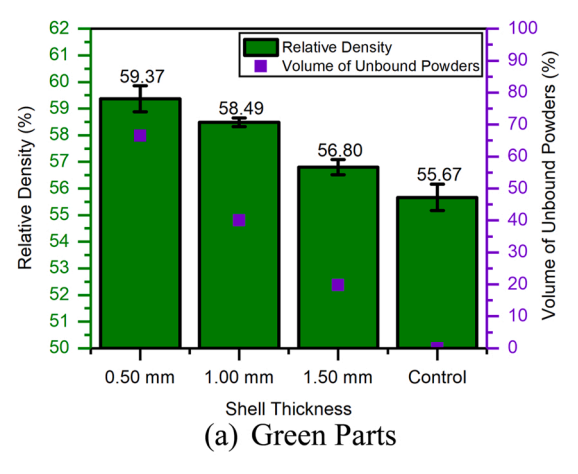
printed with identical process parameters (Table 2); the only difference between specimens is their binder content, which was achieved by applying different shell thickness.

The observed trend in sintered density of the parts indicate that minimizing binder content is beneficial for part densification. The results also show that the shell parts' densification is not only a function of the shell thickness, but also the volume of packed powders trapped inside. Thus, it is hypothesized that residue from binder pyrolysis impedes inter-particle neck formation and stymies densification.

3.2. Pore morphology and distribution

Microscopy of a representative specimen cross-section (XY plane) containing both the bound (shell) and unbound powder regions shows the resultant pore morphology and distribution in Fig. 7. Distinct variation can be observed in the pore microstructure between the bound and unbound regions (demarcated by dashed yellow line). The pore area fractions and pore size information of the two regions (measured using ImageJ software) are listed in Table 3.

In the unbound region, the powders demonstrated high densification, which is evident by the presence of very small, isolated, regularly shaped, and uniformly distributed pores. As the powders did not feature any binder, and remained closely packed by the outer shell, the particles only had to overcome the interparticle spaces to form necks and densify by pore closure. Although some pores were not fully eliminated, almost all the remaining pores spherodized and reduced in sizes. The estimated average pore size in the unbound region was 6.13 μm , and contributed 0.17% of the total layer porosity of 4.97% (Table 3). The opposite was observed in the bound region, where a high amount of inter-connected,



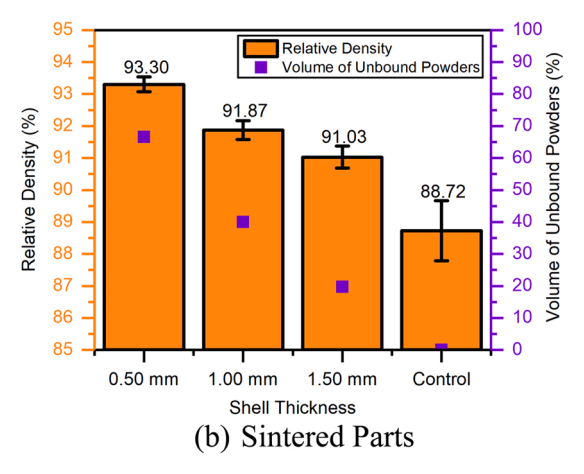


Fig. 6. Density variation with shell thickness in (a) Green Parts, and (b) Sintered Parts.

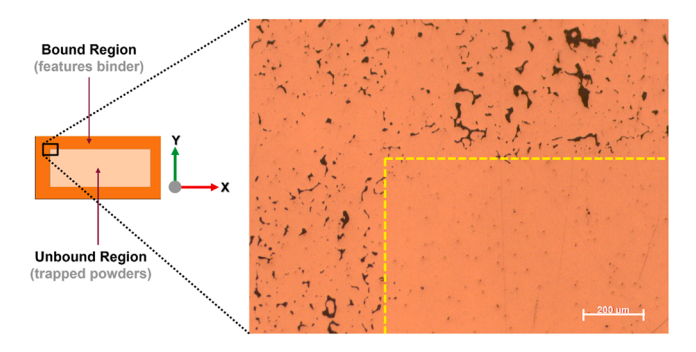


Fig. 7. Variation of pore morphology and distribution in bound and unbound interior region (as identified by a yellow dashed line) of a 1.00 mm shelled part.

Table 3 Porosity measurements of a cross-sectional layer of a shell part (t_{shell} = 1.00 mm).

| Pore Fraction (%) | Overall | 4.97 |
|------------------------|----------------|-------------------|
| | Bound Region | 4.80 |
| | Unbound Region | 0.17 |
| Average Pore Size (µm) | Bound Region | 43.50 ± 35.04 |
| | Unbound Region | 6.13 ± 2.62 |

large, irregularly shaped, and heterogeneously distributed pores can be seen. The presence of the large and irregular shaped pores indicates insufficient neck formation between particles. The binder content in this region is expected to be completely pyrolyzed before the onset of sintering densification. This strongly suggests that residue from binder burnout are trapped inside the interparticle spaces, which inhibit densification kinteics [35]. Additionally, sub-surface pores created by droplet impact during green part formation may have prevented neck formation during sintering. The estimated average pore size was 43.50 µm and the majority (4.80%) of the porosity originated from the bound region (Table 3).

It should be noted that the pore morphology and distribution in bound and unbound regions of all shelled parts were similar despite their varied shell thickness. A representative cross-sectional micrograph and porosity analysis of 1.50 mm shelled parts are provided in Fig. S1 and Table S1, respectively as supplementary information, which show similar pore morphology and distribution to that of the 1.00 mm shelled part in Fig. 7 and Table 3. This indicates that the evolution of pore morphology and distribution is an effect of the presence or absence of binder, not a function of the shell thickness.

3.3. Microstructure

Fig. 8 illustrates the optical micrographs of the etched cross-sectional surface of the bound and unbound regions of a shell part (t_{shell} = 1.00 mm). The presence of a high amount of porosity and hypothesized residue from binder burnout in the bound region retarded grain growth, resulted in much smaller grain microstructures (42.82 µm on average; Fig. 8(a)) than those found in the unbound region (166.94 µm on average; Fig. 8(b)). Many of the pores in the bound region (Fig. 8(a)) can be seen at the grain boundaries, which can be potential crack initiation sites. Additionally, some twin boundaries are observed. In contrast, the unbound region experienced significant grain growth due to the lack of binder residue and the presence of small pores (Table 3), most of which are isolated inside the grains (Fig. 8(b)).

3.4. Linear shrinkage

The linear shrinkages of the shelled and control (no shell) parts are presented in Fig. 9, and are labeled according to the coordinate system defined in Fig. 1. The control BJT printed parts (where binder is homogeneously distributed throughout the part volume) experience shrinkage consistent with that established in prior literature. Specifically, control parts see similar shrinkages in the recoating (X) and

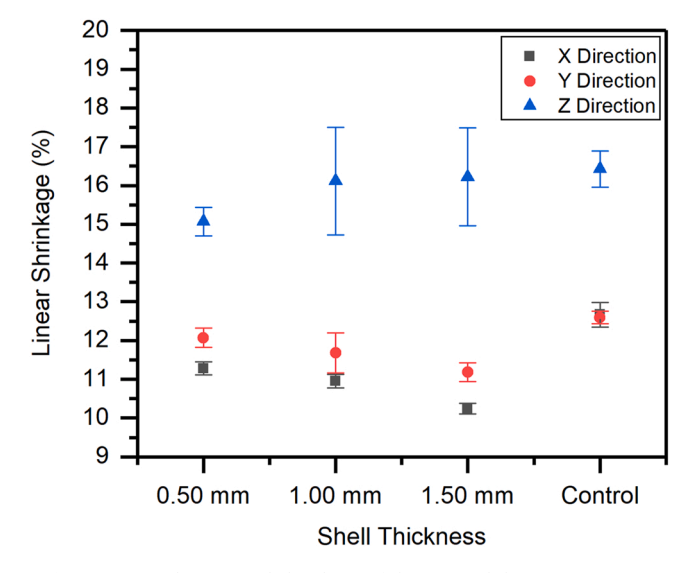
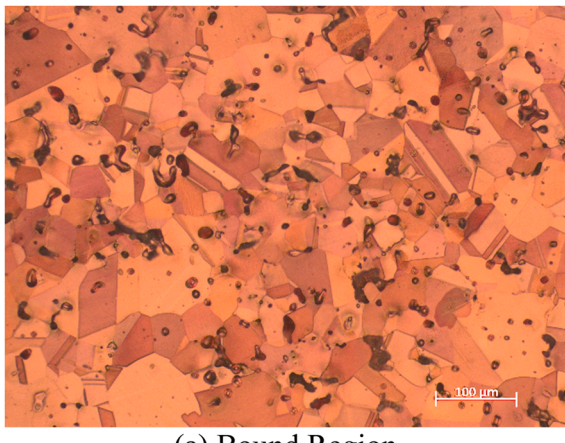
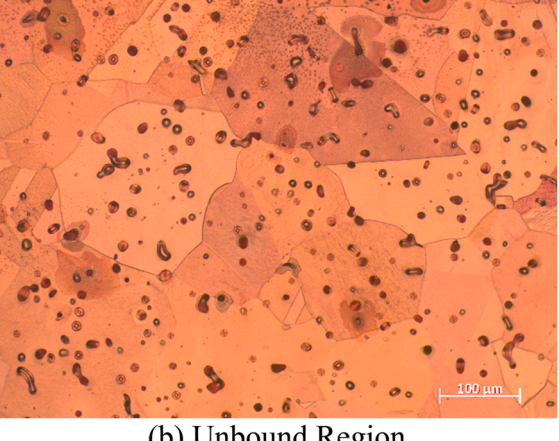


Fig. 9. Linear dimensional shrinkage of the sintered density specimens.







(b) Unbound Region

Fig. 8. Etched optical micrographs of grain microstructures of shell parts ($t_{shell} = 1.00 \text{ mm}$) (a) bound region, (b) unbound region (20x magnification).

printing (Y) directions, and larger shrinkage in the build (Z) direction [2]. The shrinkages in X and Y directions are influenced by the corresponding droplet spacings and the potential disturbances caused by the ballistic effects of droplet impacts [34,36]. In the build (Z) direction, as the polymeric binder is pyrolyzed, pores at the layer interfaces collapse due to gravity and result in higher shrinkages than in the XY plane [2, 37].

In both X and Y directions, parts with thinner shell thickness experience higher shrinkage than thicker shelled parts, due to their higher volume of unbound powder, which densifies more than bound powder. It was also observed that the shelled parts demonstrated statistically higher shrinkage in Y direction relative to X direction. It is hypothesized that the momentum of the jetted droplets disturbs the powder bed more in the Y direction (i.e., the direction of printhead movement), which creates additional porosity and results in higher shrinkages in this direction.

Similar to standard BJT parts, the Z direction shrinkage in shelled parts were significantly higher than their X and Y direction shrinkage. However, the differences of average shrinkage among the shelled parts were not statistically significant (p-value > 0.05). This suggests that shrinkage in shelled parts is dominated by the amount of unbound powder than the shell thickness itself. The thickness of unbound powders along Z direction in the specimens tested in this study are very small compared to the thicknesses of unbound powders in X and Y directions (refer to Fig. 3 overall dimensions). For example, 1.0 mm shell thickness parts have 2.5 mm of unbound powders in Z direction, compared to 25 mm in X and 7 mm in Y direction. It is hypothesized that lower unbound powder thickness in Z direction may manifest some uncertainty in the shrinkages in Z direction.

Despite having overall lower densification, the control parts experienced higher shrinkages than shelled parts in both X and Y directions. In the Z direction, only the thinnest shell (t_{shell}=0.5 mm) parts resulted in statistically less shrinkage than the control parts in Z direction. In the presented shell printing approach, the bound and unbound regions experience different densification and shrinkage behavior due to the lack/presence of binder and particle ejection induced porosity; thus, their shrinkage behavior is different than control parts which have homogenous binder concentration and densification kinetics throughout their volume. It is observed that, in general, binder pyrolysis in control parts results in larger inter-particle porosity and higher shrinkage; shell parts experience less shrinkage due to the lack of binder-induced pores while also achieving higher densification in the unbound region.

3.5. Tensile strength

Uniaxial tensile tests were performed on the printed tensile specimens (representative tensile specimens can be seen in Fig. 10) to evaluate the effect of shell printing approach, and the associated densification and grain growth, on the mechanical strength of the parts. The ultimate tensile strength, and percent elongation of the specimens are listed in Table 4. Representative fracture surface images are also included in the table.

Parts with lower shell thickness (i.e., lower binder content) demonstrated higher ultimate tensile strength. The smallest shell thickness (0.50 mm) parts demonstrated the largest strength, at 171.29 \pm 0.91 MPa. The strength decreased by at least 5.72 MPa with 0.50 mm increase in shell thickness (i.e., 1.00 mm shell thickness parts). The control (no-shell) specimens provided the lowest strength, at 157.38 \pm 0.85 MPa. Similarly, parts with lower binder content demonstrated higher elongation.

It is worth noting that parts with finer grains typically have higher grain boundary to dislocation ratio, which can lead to higher strength according to Hall-Petch relationship [38–40]. Thus, it would suggest that control (no-shell) parts would show the largest strength (Fig. 8). However, a sharp gradient of grain sizes is present in all of the shell parts in this study. Specimens with larger shell thickness feature a higher



Fig. 10. Sintered tensile specimens with 0.50 mm shell thickness.

Table 4Tensile strength of printed parts

| Tensile strength of printed parts. | | | | | |
|------------------------------------|--|------------------|------------------|--|--|
| Specimen/ Shell Thickness | Ultimate Tensile Strength (MPa) | Elongation (%) | Fracture Surface | | |
| 0.50 mm | 171.29 ± 0.91 | 50.63 ± 3.34 | — 1 mm | | |
| 1.00 mm | 165.57 ± 2.47 | 47.84 ± 0.64 | — 1 mm | | |
| Control (No- shell) | 157.38 ± 0.85 | 45.97 ± 3.21 | 1 mm | | |

number of smaller grains in the bound region and relatively lower number of large grains in the unbound region as compared to the specimens with smaller shell thickness. However, the presence of significant amount of porosity in the bound region diminishes the effects of grain boundary to dislocation ratio, resulting in lower strength in larger shell thickness and control parts. Therefore, porosity acts as the dominant influencing factor in determining the strength of the parts.

Previous work in BJT of $30+5~\mu m$ bimodal copper powders printed with traditional (no-shell) approach demonstrated tensile strength of 144.9 MPa with ductility of 17.90% [25,41]. The strength and ductility were improved in a later study using fine copper powders (D50: $5~\mu m$), which had an ultimate tensile strength of $162.70\pm3.40~MPa$ and ductility of 42.20% [31]. A similar or better performance has been achieved by the shell printing approach in this study using $30+5~\mu m$

powders. This clearly indicates that shell printing approach could be beneficial for improving quality of BJT of metal parts.

3.6. Residual carbon content

The results presented in previous sections showed that parts containing higher binder content (i.e., larger shells) featured lower sintered density and ultimate tensile strength than parts with lesser binder content. Additionally, the bound region resulted in high porosity (4.8%) and large pores (43.50 \pm 35.04; Table 3) at the grain boundaries (Fig. 8(a)), whereas the unbound region had lower porosity (0.17%) and smaller pores (6.13 \pm 2.62) located mostly inside the grains (Fig. 8(b)). These differences are hypothesized to be due to the presence of binder residue in the parts, which inhibit sintering densification.

To verify this hypothesis, EDS was performed on a cross-section of a sintered shelled part to evaluate the presence of residual carbon in the bound (i.e., shell) and unbound (i.e., packed trapped powders) regions. Fig. 11(a) shows the SEM micrograph of the surface containing both bound and unbound regions (the dashed yellow line represents the interface of the two regions) where EDS was performed. As shown in Fig. 11(b, c, d, e), the elemental mappings indicate the presence of a high amount of carbon at the pores in the bound region, whereas no carbon was observed in the unbound region. Some extent of oxidation of the metallographic surface occurred after the sample preparation, as evident

by the presence of oxygen as secondary element (Fig. 11(d)).

Elemental analysis on three locations (inside grain, on grain boundary, and at the pore) in the bound region was performed to evaluate the elemental composition (Fig. 12). The corresponding spectrum and composition are provided in Fig. 12(b, c, d). As can be seen in the inset tables, no carbon is observed inside the grain (Fig. 12(b)), and a trace amount of carbon was observed on the grain boundary (Fig. 12(c)), while the pore contained the highest amount of carbon (Fig. 12(d)).

To determine the relative amount of binder residue (in the form of carbon) in the bulk material of sintered shelled parts, optical emission spectroscopy (OES) was performed on the part surfaces, which are given in Table 5. The carbon contents reported are based on OES on three spots on each part surface. Parts with smaller shell thickness (i.e., lower binder content) demonstrate lower residual carbon content. It is worth reiterating that these parts have gone through identical processing with the only difference being the binder content, which was achieved by different shell thicknesses. The results validate that parts with more binder content have more carbon residue.

3.7. Part stability

In BJT, the binder provides structural integrity to the green parts to enable cleaning and depowdering. The resultant residue from pyrolysis also provides some stability to the powder form before sintering can

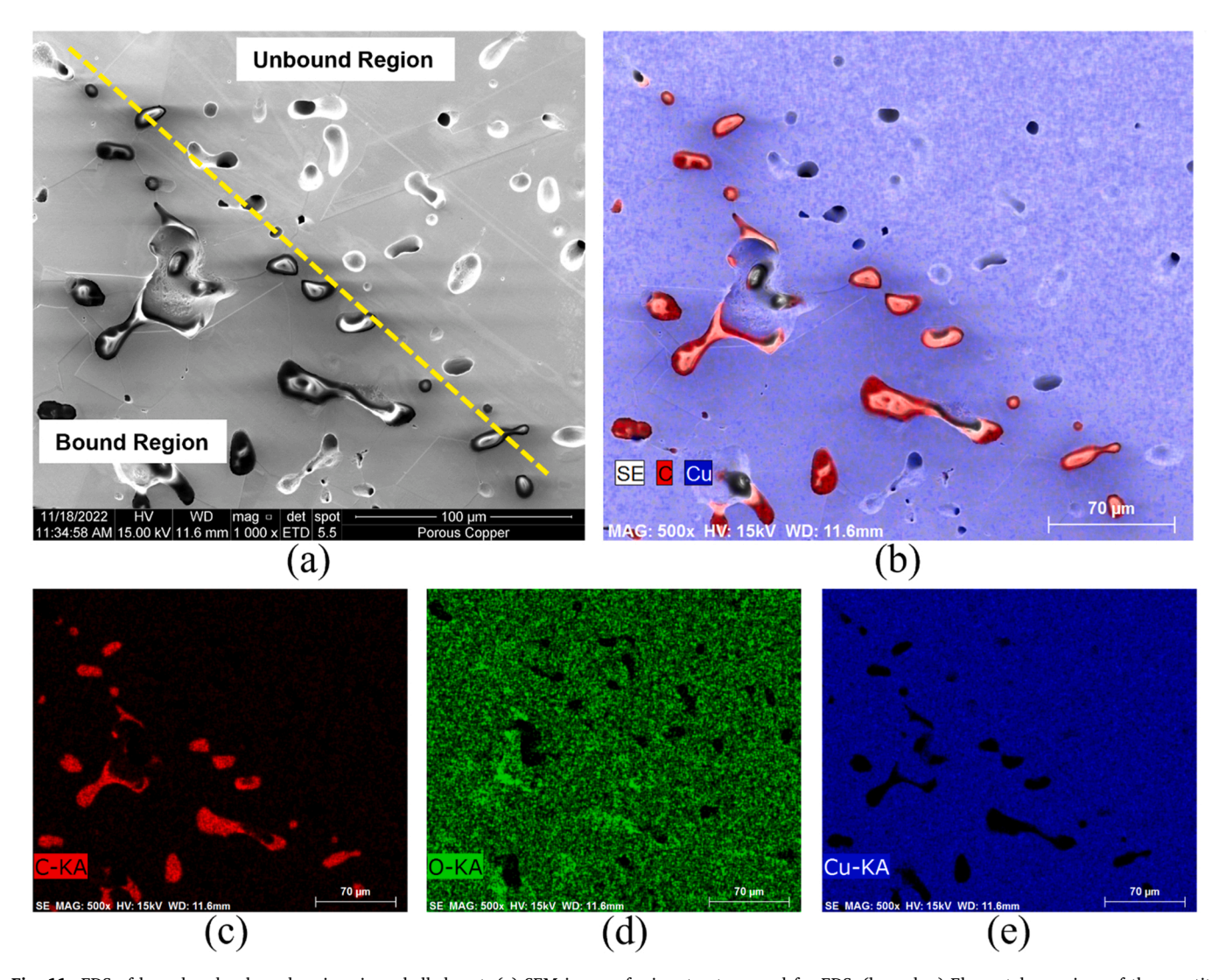


Fig. 11. EDS of bound and unbound regions in a shelled part. (a) SEM image of microstructure used for EDS, (b, c, d, e) Elemental mappings of the constituent materials.

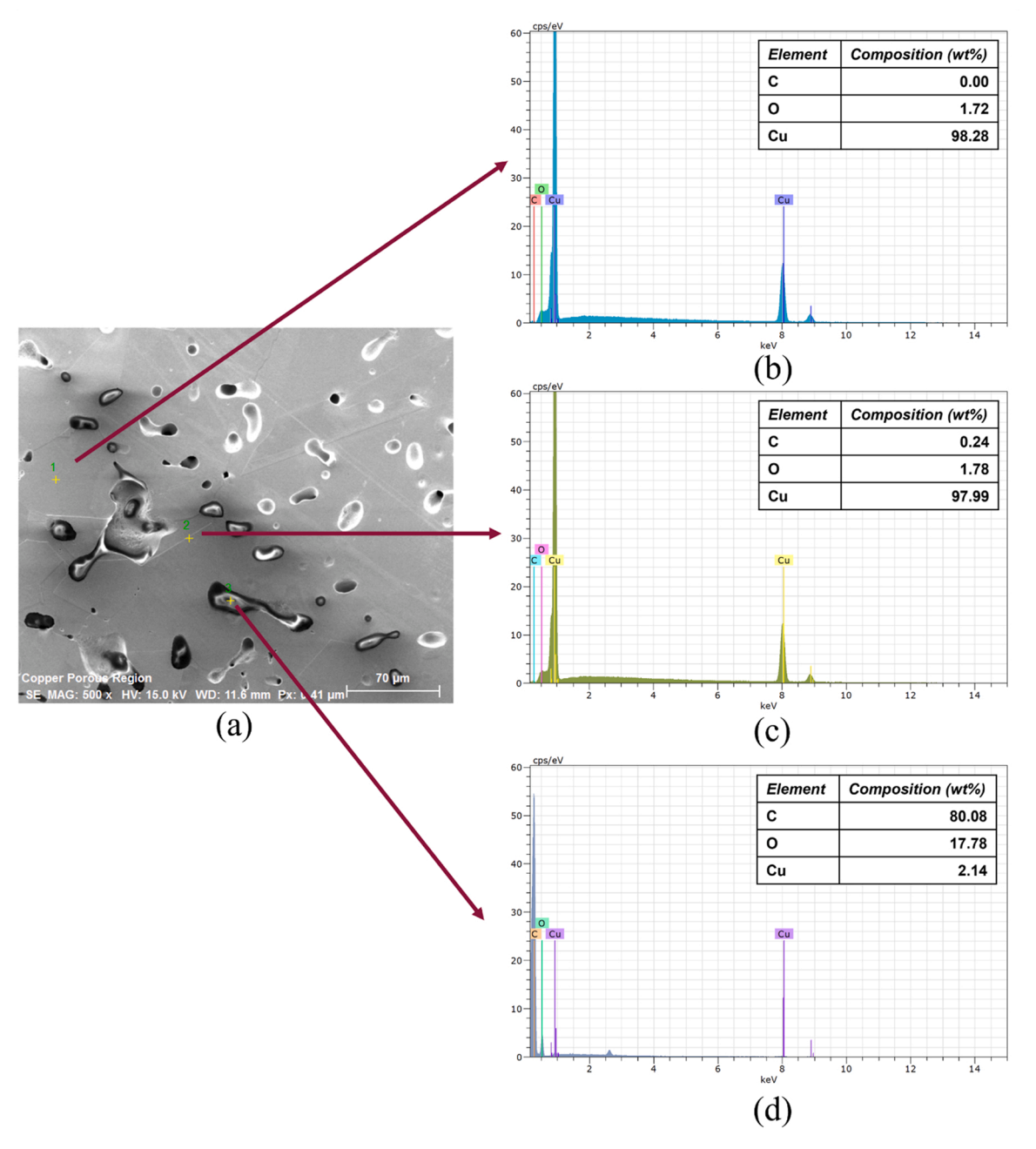


Fig. 12. Elemental composition at different locations in the bound microstructure (a) micrograph with locations marked, and spectrum (b) inside the grain, (c) on the grain boundary, and (d) at the pore. The inset tables provide corresponding composition of elements.

Table 5Residual carbon content in shell parts measured through optical emission microscopy.

| Specimen | Carbon Content (wt%) | Standard Deviation | |
|----------|----------------------|--------------------|--|
| 0.50 mm | 0.0063 | 0.0005 | |
| 1.00 mm | 0.01 | 0.0024 | |
| 1.50 mm | 0.012 | 0.0028 | |
| Control | 0.014 | 0.001 | |

begin. While shell printing has demonstrated improved final part properties, there is concern that its reduced binder content can negatively affect the stability of parts during sintering. Therefore, it is essential to evaluate the effectiveness in maintaining stability of the parts. For this evaluation, parts with a cantilevered feature (inspired by

[9]) were designed having varying shell thicknesses (Fig. 3). The printed parts were then sintered. Deflection of the cantilever due to slumping was then evaluated (Fig. 13).

Fig. 14 illustrates the details of the slumping test results. It was found that all of the overhang features experienced slumping, regardless of the presence of a shell. However, the shelled parts (Fig. 14(b, d)) had visible cracks (marked with red arrow), with the thinner shell (0.50 mm) having a larger crack than the thicker shell (1.00 mm) at the top section. The cantilever feature imposed a bending stress at the top section, creating a tension force. In conventional BJT, in which binder is homogenously distributed throughout the part volume, the presence of binder in the green part can help in counteracting the tension; however, that support diminishes as the binder starts leaving the part during burnout step, resulting in slumping (as can be seen in Fig. 14(e)). As shell parts feature less binder (and thus less residual carbon) than the



(a) Before Sintering

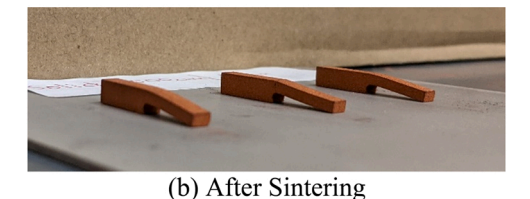


Fig. 13. Slumping test of overhang features (from left to right: $t_{shell}=0$, 0.50 mm, 1.00 mm).

control part, there is less overall support following debinding (confirmed in Fig. 11), which leads to additional slumping and cracking during sintering. Investigating additional post-processing parameters and other strategies for addressing the tradeoff between the additional densification and slumping found in shell printing is a focus of future work.

4. Summary and future work

In this study, "shell printing" has been studied as a new concept to BJT, in which a shell of bound powder surrounds a core of unbound powder. In addition to improving the final part properties, this selective

deposition of binder unveiled the impacts of binder in BJT part densification. The process-structure-properties relationships presented in this study offer important insights on the role of binder in BJT. Through this study, it was discovered that:

- Pores in bound regions are larger, irregular, and heterogeneously distributed, while they are smaller, regular, and homogeneously distributed in unbound region. Additionally, the pore fraction in bound region featured 4.80% porosity, compared to 0.17% in unbound region. This porosity was independent of shell thickness.
- The grain microstructures are smaller in the bound region (42.82 μ m) than unbound region (166.94 μ m).
- Parts with lower binder content (i.e., smaller shell thickness) demonstrated lower residual carbon (Table 5).
- Unbound regions featured almost no residual carbon and significantly higher densification, as compared to bound regions, which featured substantially more residual carbon and large pores (Figs. 11 and 12).
- The sintered density of the parts increased as shell thickness (i.e., bound volume) is decreased. The degree of densification is dependent on the volume of "unbound" powders relative to the bound powders. In this case, a 0.50 mm shell thickness provided the highest sintered density of 93.30% (which is the largest for any BJT printed pure copper parts reported in literature without using HIP or adding a sintering densifier).
- The use of shell printing improves the tensile strength and ductility of the parts, with 0.50 mm shell thickness providing the highest strength (171.29 \pm 0.91 MPa) and ductility (50.63% elongation).

Based on the findings of the shell printing study, the following fundamental conclusions were drawn on the impact of binder on BJT

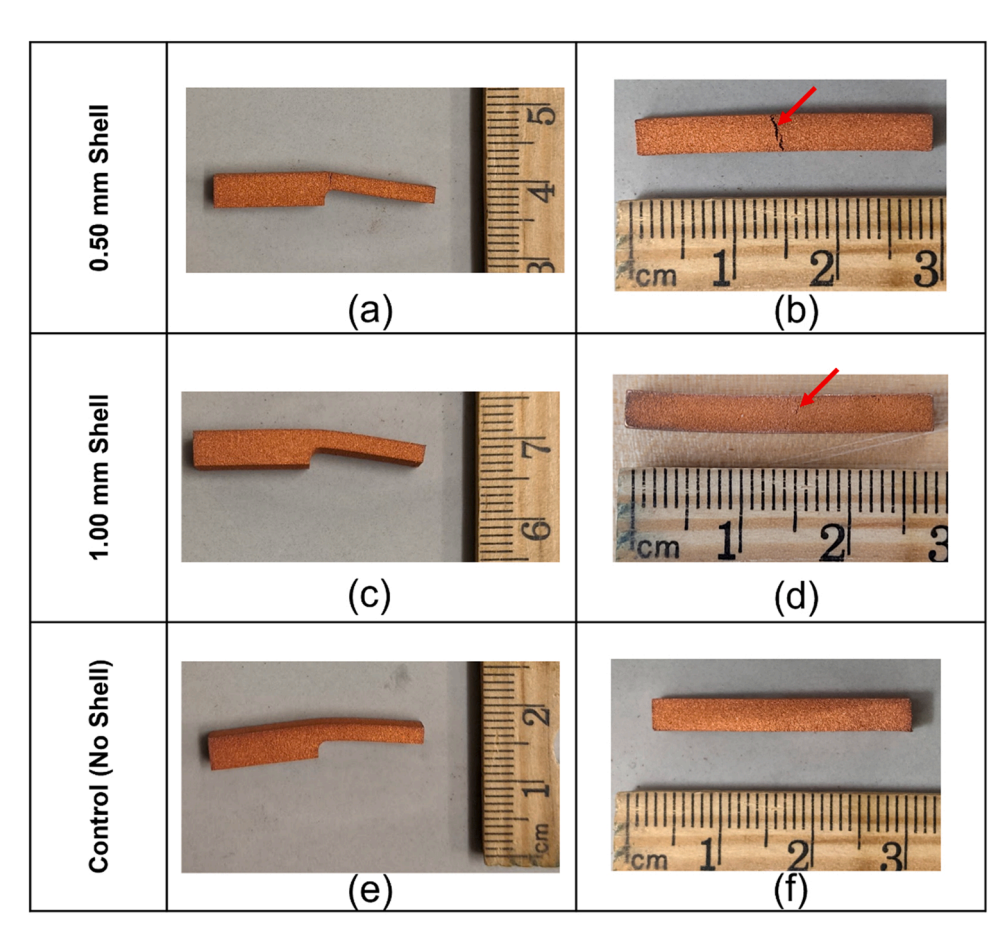


Fig. 14. Slumping test results.

part densification:

- Although binder ensures particle bonding and part shape definition, it adversely affects densification.
- Presence of binder in the part induces porosity during sintering.
- Grain growth is retarded by the presence of binder residue during sintering.
- Presence of binder residue provides structural stability and minimizes slumping of overhanging features before sintering begins.

The presented "shell printing" approach has demonstrated enhanced properties in BJT printed parts. While the printed green shell specimens evaluated in this study were sufficiently strong for post-processing handling, thin shells (e.g., $t_{\rm shell}=0.50$ mm) might not be sufficient for large, complex parts. Therefore, future studies will focus on evaluating green strength of shell parts, and if necessary, design for additive manufacturing (DfAM) strategies on how to account for the tradeoff between enhanced sintered part properties and weaker green part properties. If the enhanced part properties enabled by shell printing approach are desired, part features will also have to be carefully designed to mitigate slumping in overhang features. For example, during sintering, support fixtures could be used, and parts should be oriented appropriately to minimize slumping.

In addition, this study was conducted with one type (ExOne Aquafuse) of binder; future work should investigate other binders. The authors hypothesize that any polymeric binder with a carbon backbone will have similar effects as seen this study, perhaps at different scales. Unraveling the pore evolution and densification in the bound and unbound regions through X-ray computed tomography (e.g., [42]) could offer deeper insights on the impact of binder and should be part of future study. Such insight could offer a pathway towards further tailoring of porosity and grain microstructure in binder jetted parts.

CRediT authorship contribution statement

Kazi Moshiur Rahman: Writing – review & editing, Writing – original draft, Visualization, Validation, Methodology, Investigation, Formal analysis, Data curation, Conceptualization. Amanda Wei: Writing – review & editing, Validation, Methodology, Investigation. Hadi Miyanaji: Validation, Methodology, Investigation, Conceptualization. Christopher Bryant Williams: Writing – review & editing, Supervision, Resources, Project administration, Methodology, Funding acquisition, Conceptualization.

Declaration of Competing Interest

The authors declare that they have no known competing financial interests or personal relationships that could have appeared to influence the work reported in this paper.

Data Availability

Data will be made available on request.

Acknowledgements

This material is based upon work supported by the National Science Foundation under Grant No. 1932213. The authors also acknowledge the Department of the Navy award number N00014–19-1–2736 issued by the Office of Naval Research for financial support. The United States Government has a royalty-free license throughout the world in all copyrightable material contained herein. Any opinions, findings, and conclusions or recommendations expressed in this material are those of the authors and do not necessarily reflect the views of the National Science Foundation or Office of Naval Research. The authors acknowledge the assistance from Dr. Jonathan Angle of the Nanoscale

Characterization and Fabrication Laboratory, Institute for Critical Technology and Applied Science at Virginia Tech in performing the EDS analysis and Dr. Alan Druschitz of Virginia Tech Foundry Institute for Research and Education in performing the OES on the specimens.

Appendix A. Supporting information

Supplementary data associated with this article can be found in the online version at doi:10.1016/j.addma.2022.103377.

References

- [1] I. Gibson, et al., Additive Manufacturing Technologies, Springer, 2021.
- [2] A. Mostafaei, et al., Binder jet 3D printing- process parameters, materials, properties, modeling, and challenges, Prog. Mater. Sci. vol. 119 (2021), 100707.
- [3] H. Miyanaji, N. Momenzadeh, L. Yang, Effect of powder characteristics on parts fabricated via binder jetting process, Rapid Prototyp. J. vol. 25 (2) (2019) 332–342, https://doi.org/10.1108/rpj-03-2018-0069.
- [4] H. Miyanaji, S. Zhang, L. Yang, A new physics-based model for equilibrium saturation determination in binder jetting additive manufacturing process, Int. J. Mach. Tools Manuf. vol. 124 (2018) 1–11, https://doi.org/10.1016/j. ijmachtools.2017.09.001.
- [5] B. Derby, Inkjet printing of functional and structural materials: fluid property requirements, feature stability, and resolution, Annu. Rev. Mater. Res. vol. 40 (2010) 395–414.
- [6] Y. Bai, C. Wall, H. Pham, A. Esker, C.B. Williams, Characterizing binder–powder interaction in binder jetting additive manufacturing via sessile drop goniometry, J. Manuf. Sci. Eng. vol. 141 (1) (2018), https://doi.org/10.1115/1.4041624.
- [7] A. Mostafaei, P.R. De Vecchis, A.K. Katerina, D. Elhassid, M. Chmielus, Effect of binder saturation and drying time on microstructure and resulting properties of sinter-HIP binder-jet 3D-printed WC-Co composites, Addit. Manuf. (2021), 102128.
- [8] R. Jiang, L. Monteil, K. Kimes, A. Mostafaei, M. Chmielus, Influence of powder type and binder saturation on binder jet 3D-printed and sintered Inconel 625 samples, Int. J. Adv. Manuf. Technol. vol. 116 (11) (2021) 3827–3838.
- [9] Y. Bai, C.B. Williams, The effect of inkjetted nanoparticles on metal part properties in binder jetting additive manufacturing, Nanotechnology vol. 29 (39) (2018), 395706.
- [10] H. Chen, Y.F. Zhao, Process parameters optimization for improving surface quality and manufacturing accuracy of binder jetting additive manufacturing process, Rapid Prototyp. J. (2016).
- [11] K.J. Hodder, J.A. Nychka, R.J. Chalaturnyk, Process limitations of 3D printing model rock, Prog. Addit. Manuf. vol. 3 (3) (2018) 173–182.
- [12] M. Vaezi, C.K. Chua, Effects of layer thickness and binder saturation level parameters on 3D printing process, Int. J. Adv. Manuf. Technol. vol. 53 (1) (2011) 275–284
- [13] R.K. Enneti, K.C. Prough, Effect of binder saturation and powder layer thickness on the green strength of the binder jet 3D printing (BJ3DP) WC-12% Co powders, Int. J. Refract. Met. Hard Mater. vol. 84 (2019), 104991.
- [14] M. Castilho, B. Gouveia, I. Pires, J. Rodrigues, M. Pereira, The role of shell/core saturation level on the accuracy and mechanical characteristics of porous calcium phosphate models produced by 3Dprinting, Rapid Prototyp. J. vol. 21 (1) (2015) 43–55.
- [15] H. Miyanaji and L. Yang, Equilibrium Saturation in Binder Jetting Additive Manufacturing Processes: Theoretical Model vs Experimental Observations, in 2016 International Solid Freeform Fabrication Symposium, 2016: University of Texas at Austin.
- [16] K. Lu, W.T. Reynolds, 3DP process for fine mesh structure printing, Powder Technol. vol. 187 (1) (2008) 11–18.
- [17] N. Lecis, et al., Effects of process parameters, debinding and sintering on the microstructure of 316L stainless steel produced by binder jetting, Mater. Sci. Eng.: A vol. 828 (2021), 142108.
- [18] S. Shrestha, G. Manogharan, Optimization of binder jetting using Taguchi method, Jom vol. 69 (3) (2017) 491–497.
- [19] Y. Bai, C.B. Williams, Binder jetting additive manufacturing with a particle-free metal ink as a binder precursor, Mater. Des. vol. 147 (2018) 146–156.
- [20] J.G. Bai, K.D. Creehan, H.A. Kuhn, Inkjet printable nanosilver suspensions for enhanced sintering quality in rapid manufacturing, Nanotechnology vol. 18 (18) (2007), 185701.
- [21] N. Reis, C. Ainsley, B. Derby, Ink-jet delivery of particle suspensions by piezoelectric droplet ejectors, J. Appl. Phys. vol. 97 (9) (2005), 094903.
- [22] B. Derby, N. Reis, Inkjet printing of highly loaded particulate suspensions, MRS Bull. vol. 28 (11) (2003) 815–818.
- [23] A. Du Plessis, et al., Productivity enhancement of laser powder bed fusion using compensated shelled geometries and hot isostatic pressing, Adv. Ind. Manuf. Eng. vol. 2 (2021), 100031.
- [24] P.D. Prichard, K. Gamble, and J. Skwara, Additive manufacturing techniques and applications thereof, US Patent Appl. 15/831,779, 2019.
- [25] Y. Bai, G. Wagner, C.B. Williams, Effect of particle size distribution on powder packing and sintering in binder jetting additive manufacturing of metals, J. Manuf. Sci. Eng. vol. 139 (8) (2017), https://doi.org/10.1115/1.4036640.
- [26] R.M. German, Prediction of sintered density for bimodal powder mixtures, Metall. Trans. A vol. 23 (5) (1992) 1455–1465.

- [27] J.H. Tan, W.L.E. Wong, K.W. Dalgarno, An overview of powder granulometry on feedstock and part performance in the selective laser melting process, Addit. Manuf. vol. 18 (2017) 228–255.
- [28] A.M. Elliott, P. Nandwana, D.H. Siddel, B. Compton, A Method for Measuring Powder Bed Density in Binder Jet Additive Manufacturing Process and the Powder Feedstock Characteristics Influencing the Powder Bed Density, Oak Ridge National Lab. (ORNL), Oak Ridge, TN (United States), 2016.
- [29] B-925-15, Standard Practices for Production and Preparation of Powder Metallurgy (PM) Test Specimens, A. International, 2016.
- [30] E.M. Sachs et al., "Jetting layers of powder and the formation of fine powder beds thereby," US Patent 6,596,224, 2003.
- [31] H. Miyanaji, K.M. Rahman, M. Da, C.B. Williams, Effect of fine powder particles on quality of binder jetting parts, Addit. Manuf. vol. 36 (2020), 101587.
- [32] Y. Bai, C.B. Williams, An exploration of binder jetting of copper, Rapid Prototyp. J. vol. 21 (2) (2015) 177–185, https://doi.org/10.1108/rpj-12-2014-0180.
- [33] B962–17, Standard Test Methods for Density of Compacted or Sintered Powder Metallurgy (PM) Products Using Archimedes' Principle, A. International, 2017.
- [34] N.D. Parab, et al., Real time observation of binder jetting printing process using high-speed X-ray imaging, Sci. Rep. vol. 9 (1) (2019) 1–10.
- [35] Y. Wu, R. German, D. Blaine, B. Marx, C. Schlaefer, Effects of residual carbon content on sintering shrinkage, microstructure and mechanical properties of

- injection molded 17-4 PH stainless steel, J. Mater. Sci. vol. 37 (17) (2002) 3573-3583
- [36] M. Jamalkhani, et al., Deciphering microstructure-defect-property relationships of vacuum-sintered binder jetted fine 316 L austenitic stainless steel powder, Addit. Manuf. vol. 59 (2022), 103133.
- [37] A. Mostafaei, P.R. De Vecchis, I. Nettleship, M. Chmielus, Effect of powder size distribution on densification and microstructural evolution of binder-jet 3D-printed alloy 625, Mater. Des. vol. 162 (2019) 375–383.
- [38] E. Hall, The deformation and ageing of mild steel: III discussion of results, Proc. Phys. Soc. Sect. B vol. 64 (9) (1951) 747.
- [39] N. Petch, The cleavage strength of polycrystals, J. Iron Steel Inst. vol. 174 (1953) 25–28.
- [40] N. Hansen, Hall–Petch relation and boundary strengthening, Scr. Mater. vol. 51 (8) (2004) 801–806.
- [41] A.Y. Kumar, Y. Bai, A. Eklund, C.B. Williams, The effects of Hot Isostatic Pressing on parts fabricated by binder jetting additive manufacturing, Addit. Manuf. vol. 24 (2018) 115–124.
- [42] Y. Zhu, Z. Wu, W.D. Hartley, J.M. Sietins, C.B. Williams, Z.Y. Hang, Unraveling pore evolution in post-processing of binder jetting materials: X-ray computed tomography, computer vision, and machine learning, Addit. Manuf. vol. 34 (2020), 101183